Room-Temperature Crystallization of Hybrid-Perovskite Thin Films *via* Solvent-Solvent Extraction for High-Performance Solar Cells †

Yuanyuan Zhou,[a] Mengjin Yang,[b] Wenwen Wu,[a] Alexander L. Vasiliev,[a,§]
Kai Zhu [b,*] and Nitin P. Padture [a,*]

[a] School of Engineering, Brown University, Providence, RI 02912, USA.
Email: nitin_padture@brown.edu

[b] Chemical and Materials Science Center, National Renewal Energy Laboratory, Golden, CO
80401, USA. Email: kai.zhu@nrel.gov

Journal of Materials Chemistry A (Full Paper)

Abstract

The room-temperature solvent-solvent extraction (SSE) concept is used for the deposition of hybrid-perovskite thin films over large areas. In this simple process, perovskite precursor solution is spin-coated onto a substrate, and instead of the conventional thermal annealing treatment, the coated substrate is immediately immersed in a bath of another solvent at room temperature. This results in efficient extraction of the precursor-solvent and induces rapid crystallization of uniform, ultra-smooth perovskite thin films. The mechanisms involved in the SSE process are elucidated, and its versatility in depositing high quality thin films of controlled thicknesses (20 to 700 nm) and various compositions ($CH_3NH_3PbI_{(3-x)}Br_x$; x = 0, 1, 2, or 3) is demonstrated. Planar perovskite solar cells (PSCs) based on SSE-deposited $CH_3NH_3PbI_3$ perovskite thin films deliver power conversion efficiency (PCE) up to 15.2%, and most notably an average PCE of 10.1% for PSCs with sub-100 nm semi-transparent perovskite thin films. The SSE method has generic appeal, and its key attributes — room-temperature process, rapid crystallization, large-area uniform deposition, film-thickness control, ultra-smoothness, and compositional versatility — make the SSE method potentially suitable for roll-to-roll scalable processing of hybrid-perovskite thin films for future multifunctional PSCs.

Graphical Abstract

A simple one-step solvent-bathing process based on solvent-solvent extraction, is demonstrated for the controlled room-temperature crystallization of uniform, smooth hybrid-perovskite thin films for high-efficiency solar cells.
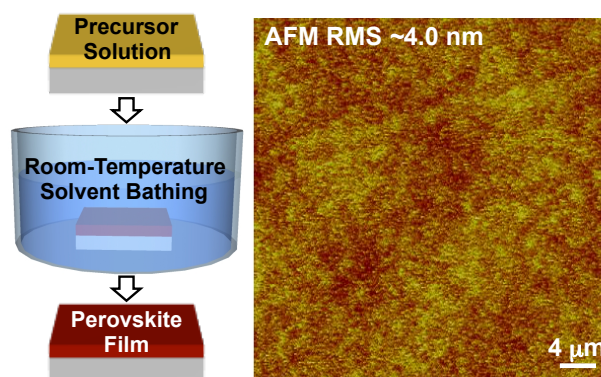
Introduction

The field of thin-film photovoltaics is witnessing a revolution of sorts with the advent of perovskite solar cells (PSCs) that use hybrid perovskites as the light absorber,[1-5] and now the power conversion efficiency (PCE) of PSCs has exceeded 20%.[6] While hybrid perovskites are a family of organometallic halides with the general formula $RMeX_3$ (R = organic group, Me = Pb or Sn, and X = I, Br, Cl or a combination),[7] methylammonium (MA) lead triiodide ($CH_3NH_3PbI_3$ or $MAPbI_3$) is the most studied in the context of PSCs.[1-5]

Typically, solution processing of perovskite films in PSCs is carried out using the one-step method[8-11] or the two- step method,[10-13] and variations thereof. In the simplest one-step method, the precursors (*e.g.* MAI and PbX_2) are dissolved together in a polar solvent, such as dimethylformamide (DMF), dimethysulfoxide (DMSO), γ-butyrolactone (GBL), or N-methyl-2-pyrrolidone (NMP), and spin-coated. This is invariably followed by heating the film at 70-150 ˚C to evaporate the high-boiling-point solvent. It has been suggested that the reaction $PbI_2+MAI{\rightarrow}MAPbI_3$, and the concomitant crystallization of $MAPbI_3$ perovskite, occur during this heating step.[8] However, the direct formation of the perovskite from solutions at the elevated temperature is difficult to control. To address this issue, the two-step method was developed, which entails dipping of a solution-deposited PbI_2 thin film in a MAI solution, or spin-coating MAI solution on top of the PbI_2 film, followed by heat-treatment at 70-150 ˚C. Several other processing strategies have been employed to improve further the quality of the perovskite films, including solvent engineering,[14] fast deposition-crystallization (FDC),[15] gas-blowing,[16], successive spin-coating/annealing,[17,18] and solvent washing.[19] However, all these solution methods involve some heat-treatment in order to evaporate the solvent and/or crystallize the perovskite films. Vapour-based methods, either all-vapour[20-22] or combined with solution-methods,[23, 24] are also used for depositing perovskite thin films, but the need for specialized equipment and batch-processing present fundamental limitations to processing scalability. Furthermore, deposition of full-coverage perovskite films with controlled thicknesses, especially semitransparent films of sub-100 nm thickness, is difficult in both solution- and vapour-based methods.[22]

In this context, we demonstrate here the use of the solvent-solvent extraction (SSE) concept for the room-temperature solution processing of high quality hybrid-perovskite thin films that are uniform over a large area. The SSE approach allows exquisite control over film thickness, and since the perovskite crystallization occurs at room-temperature and it is very rapid, the SSE process is potentially scalable. The SSE process is depicted schematically in Fig. 1, where in the case of deposition of the popular hybrid perovskite $MAPbI_3$, a stoichiometric $MAPbI_3$ solution in NMP — a high-boiling-point (204 ˚C) polar solvent — is spin-coated. (Other methods, such as dip-coating, spraying, or inkjet-printing, may also be used to deposit the $MAPbI_3$ precursor solution.) This is similar to the conventional one-step method mentioned earlier, but in SSE, instead of heating, the clear spin-coated $MAPbI_3$ precursor thin film is immersed immediately into a room-temperature bath of diethyl ether ($C_2H_5OC_2H_5$ or DEE) — a low-boiling-point (35 ˚C) solvent. The $MAPbI_3$ thin film deposits within two minutes, and it is then taken out of the bath and dried at room temperature, with no further heat-treatment.

Note that the FDC approach for the deposition of planar $MAPbI_3$ perovskite thin films reported by Xiao *et al.*[15] uses a similar concept. However, they drip the second solvent at certain times during the high-speed spin-coating of $MAPbI_3$ precursor solution in DMF, instead of solvent bathing used in our SSE approach. This makes the FDC method less controllable in achieving large-area uniformity in the perovskite thin films. Also, the partial extraction of the

solution-solvent during spin-coating steps in FDC, and the use of higher boiling-point second solvents (*e.g.* chlorobenzene, boiling point 131 °C), necessitate heat-treatment at 100 °C to evaporate any residual solvent and to promote further crystallization.[15] Jeon *et al.*[14] have also used dripping of a second solvent (toluene; boiling point 111 °C) to "freeze" the solution-solvent and perovskite precursor into an intermediate state. That process also requires heat-treatment (at 100 °C) in order to produce $MAPbI_{(3-x)}Br_x$ (*x*=0.3-0.45) perovskite films (~200 nm) in mesoporous TiO_2. Most recently, Jung *et al.*[19] have used toluene, chlorobenzene, or dicholorobenzene (boiling point 174 °C) as the second solvent (dripped), with reduced heat-treatment temperatures of 60-90 °C for depositing ~300-nm thick films of $MAPbI_3$ perovskite. In this context, the use of a simpler solvent-bathing step, and the NMP-DEE solvents combination, in our SSE method enables the room-temperature deposition of perovskite thin films with excellent control over their thickness and smoothness.

Experimental
Room-temperature SSE deposition of perovskite thin films

All reagent grade chemicals were obtained commercially from Sigma-Aldrich (St. Louis, MO) unless noted otherwise. MAI was prepared using a process described elsewhere.[25] In a typical procedure, 24 ml of 33 wt% CH_3NH_2 solution in anhydrous ethanol was reacted with 10 ml of 57 wt% HI in water, in 100 ml of ethanol (excess CH_3NH_2) in a dry Ar atmosphere at room temperature. The solvent and the excess CH_3NH_2 were removed using a rotary evaporator, and the resulting MAI powder was harvested. The same procedure was followed for the preparation of MABr, except HI was replaced by HBr. For typical preparation of $MAPbI_3$ perovskite thin films using the SSE method, first, a solution of PbI_2 (Alfa-Aesar, Ward Hill, MA) and MAI from above (molar ratio 1:1) in NMP was spin-coated onto previously patterned fluorine-doped tin oxide (FTO) coated glass substrates (TEC 15, Hartford Glass Co., Hartford City, IN), and the solution-coated substrate was vertically dipped in a ~50 ml anhydrous DEE (Fisher Scientific, Fair Lawn, NJ) bath immediately (~2 l bath in the case of larger substrates). The substrate was kept immersed until a brown film formed in ~2 min. The substrate was then taken out of the bath and dried rapidly at room temperature using blowing N_2 gas. The entire perovskite film fabrication process was performed in the ambient with ~30% humidity. The thickness of the resultant perovskite film was easily controlled by varying the perovskite solution concentration and the spinning rate. Films of thickness ~20 nm, ~80 nm, and ~250 nm were processed using 15 wt%, 30 wt%, and 42 wt% solutions at 6000 rpm (10 s), 6000 rpm (10 s), and 4500 rpm (15 s), respectively. For the preparation of $MAPbI_2Br$, $MAPbIBr_2$, and $MAPbBr_3$, the starting precursors used were $MABr:PbI_2::1:1$, $MAI:PbBr_2::1:1$, and $MABr:PbBr_2::1:1$, respectively.

Fabrication of the PSCs

For the fabrication of the PSCs, FTO-coated glass was patterned by HCl (25%) etching with Zn powder, and cleaned by soaking in a basic bath (5 wt % NaOH in ethanol) overnight. After washing with deionized water and ethanol, a compact TiO_2 blocking layer was deposited on top of patterned FTO by spray pyrolysis at 450 °C. The perovskite layer was then deposited as described above. This was followed by spin-coating a solution of hole-transporting material (HTM), which consisted of 80 mg 2,2',7,7'-tetrakis(N,N'-di-*p*-methoxyphenylamine)-9,9'-spirobifluorene (spiro-MeOTAD; Merck, Germany), 30 μl bis(trifluoromethane) sulfonimide lithium salt stock solution (500 mg Li-TFSI in 1 ml acetonitrile), 30 μl 4-tert-butylpyridine (TBP), and 1 ml chlorobenzene solvent. The HTM spin-coating process was performed in a dry-

air atmosphere with humidity below 10%. Finally a 150 nm Ag layer was deposited using thermal evaporator and a shadow mask. The PSCs were stored in a dry-air atmosphere with humidity <10%, and typically the performance of the PSCs was measured one day after their fabrication.

Film and PSC structure characterization

X-ray diffraction (XRD) was performed using a X-ray diffractometer (D-8 Discover, Bruker, Germany) with Cu Kα_1 radiation (λ=1.5406 Å) at a step size of 0.02°. XRD patterns for the confirmation of the perovskite phase were collected using a Ge (002) monochromer, at step time of 2 s. XRD patterns for tracking the SSE process used a step time of 0.1 s, without the use of the monochromer. The surface and cross-sections (fractured) morphology of thin films were characterized using a scanning electron microscope (SEM; LEO 1530VP, Carl Zeiss, Germany). Transmission electron microscopy (TEM) was used to characterize cross-sections of the as-deposited thin films and whole PSCs. Samples from specific locations on the cross-sections were prepared by focused ion beam (FIB; Helios 600, FEI, Hillsboro, OR) and *in situ* lift-out. In the case of plan-view high-resolution TEM, the SSE processed perovskite was deposited directly on Cu grids covered with holey carbon (EMS, Hatfield, PA). The SSE conditions used were identical to those used to deposit the ~80-nm MAPbI$_3$ perovskite thin films. All TEM samples were examined using TEM (2100F, JEOL, Japan) operated at 200 kV accelerating voltage. The optical spectroscopy (transmission, refection, absorption) of the thin films on TiO$_2$-blocking-layer-coated FTO was conducted on a UV-*vis*-NIR spectrophotometer equipped with diffuse reflectance accessories (Cary 6000i, Agilent Technologies, Englewood, CO) with 10 nm step size. The thin films on glass substrates were characterized using Fourier-transform infrared (FTIR) spectroscopy (4100, Jasco Instruments, Easton, MD) after 2 s and 2 min of SSE processing. Atomic force microscopy (AFM) images were obtained in tapping mode (Veeco 5000 and Nanoscope V, Plainview, NY) using a probe with tip radius of ~10 nm and a resonance frequency of ~300 kHz (AC160TS, Olympus, Japan). The AFM system is setup in an Ar glove box with H$_2$O and O$_2$ concentrations of less than 0.1 ppm.

Performance characterization of PSCs

The incident photon-to-current efficiency (IPCE) or external quantum efficiency (EQE) spectra were recorded at a chopping frequency of 5 Hz in AC mode on a solar cell quantum efficiency measurement system (QEX10, PV Measurements, Boulder, CO). The current density (*J*) - voltage (*V*) characteristics of the PSCs were obtained using a SourceMeter (2400, Keithley, Cleveland, OH) under simulated one-sun AM 1.5G illumination (100 mW cm^{-2}) (Oriel Sol3A Class AAA Solar Simulator, Newport Corporation, Irvine, CA). Typical sweeping of forward bias voltage started from 0 V to V_{OC} +50 mV and back to 0 V, at the rate of 20 mV s^{-1}, where V_{OC} is the open circuit voltage. A typical active area of 0.16 cm^2 was defined using a non-reflective mask for the *J-V* measurements. Using a procedure suggested by Snaith *et al.*,[26] the maximum-power output stability of the PSCs was measured by monitoring *J* output at the maximum-power *V* bias for up to 150 s using a VersaSTAT MC potentiostat (Princeton Applied Research, Acton, MA). A shutter was used to control the one-sun illumination on the PSC. The PSCs testing was conducted in the ambient with humidity of 20-40%. Impedance spectroscopy (IS) on the PSCs was performed using a PARSTAT 2273 workstation (Princeton Applied Research, Acton, MA) with the frequency range of 0.1 Hz to 100 kHz and the modulation amplitude of 10 mV. The IS spectra were analyzed using ZView 2.9c software (Scribner Associates, Southern Pines, NC).

Results and Discussion

SSE process description and perovskite film deposition mechanisms

As mentioned earlier, Fig. 1 depicts the SSE process schematically. Within seconds of dipping the $MAPbI_3$ precursor thin film into the DEE bath coloured specks appear on the film, and it starts to turn dark uniformly, indicating the rapid formation of $MAPbI_3$ perovskite. Within two minutes NMP solvent extraction, and the simultaneous crystallization of the $MAPbI_3$ perovskite, is complete. The thin film is then taken out from the bath and dried rapidly in ambient air. Photographs (Figs. S1-S3†) tracking the rapid film evolution are included in Electronic Supplementary Information (ESI)†.

Figure 2A shows indexed XRD pattern of a perovskite thin film deposited using the SSE method, confirming pure β-$MAPbI_3$ phase (space group *I4/mcm*[27]). Figures 2B and 2C are SEM images of top surface of a typical SSE $MAPbI_3$ perovskite thin film (~250 nm thickness) at low and high magnifications, respectively. The uniform, dense coverage is readily apparent from these SEM micrographs, with grain size of ~100 nm. The cross-sectional SEM image of a ~250 nm SSE $MAPbI_3$ perovskite thin film shows uniform coverage and a ultra-smooth film surface. The cross-section of a thinner (~80 nm) SSE $MAPbI_3$ perovskite thin film viewed in the TEM is presented in Fig. 3B, showing conformal coating of the perovskite along the rough FTO surface. Figures 3C and 3D are high-resolution TEM images of $MAPbI_3$ perovskite deposited on TEM grids using the SSE method. The ~0.44 nm and ~0.32 nm interplanar spacings in Fig. 3D correspond to (020) and (004) planes, respectively (lattice parameters *a*=*b*=8.849 Å, *c*=12.642 Å[27]), further confirming the β-$MAPbI_3$ phase. Proliferation of crystal defects are also observed in the TEM specimens made without the use of the FIB (Fig. 3C), which is typical of soft organic-inorganic hybrid materials. (Additional cross-sectional SEM and TEM images of $MAPbI_3$ perovskite thin films of thicknesses ranging from ~20 nm to ~410 nm are presented in Figs. S4† and S5†, together with cross-sectional TEM images and elemental maps of a whole PSC in Fig. S6† and S7†.)

The AFM images in Fig. 4A (40×40 μm^2) and Fig. 4B (2×2 μm^2) of the top surface of a SSE $MAPbI_3$ perovskite thin film (thickness ~250 nm) reveal root mean square (RMS) roughness of ~4.0 nm and ~5.2 nm, respectively, showing unprecedented smoothness over a large area. The highly reflective nature of the film is shown in the photograph in Fig. 4C, and the photograph in Fig. 4D demonstrates the semi-transparent nature of the SSE $MAPbI_3$ perovskite thin film over a 5×6 cm^2 area viewed in bright sunshine due to reduced light scattering on the smooth film surface. (Optical photos, transmission, reflection, and absorption spectra of SSE $MAPbI_3$ perovskite films of various thicknesses are presented in Fig. S8†.)

All the above results demonstrate the high quality of the $MAPbI_3$ perovskite thin films deposited using the room-temperature SSE method in terms of phase purity, large-area coverage, thickness range/uniformity, ultra-smoothness, and semi-transparency. It appears that mechanisms similar to those found in solvent-extraction[28] are operative in the SSE process.

To gain insight into the SSE process, XRD patterns following the progression of the SSE deposition process are shown in Figs. 5A to 5C. Figure 5A shows featureless XRD pattern from the as-spin-coated $MAPbI_3$ precursor solution thin film, while Fig. 5B shows the formation of $MAPbI_3$ perovskite after 2 s of NMP-solvent extraction. Upon further NMP extraction (2 min), the XRD pattern becomes sharper, where the strongest reflection in Fig. 5C is narrower (FWHM 2θ ~0.31°) compared to that in Fig. 5B (FWHM 2θ ~0.61°), showing the formation of phase-pure β-$MAPbI_3$ perovskite (film thickness ~250 nm). Fourier-transform infrared (FTIR) spectra from the films corresponding to Fig. 5B (2 s) and Fig. 5C (2 min) are presented in Fig. 5D. The

presence of C=O stretching band at ~1700 cm^{-1} [29] in the 2 s spectrum (red) is indicative of the presence of some NMP remaining in the thin film, but it disappears in the fully solvent-extracted thin film at 2 min (black). Based on these observations it appears that, as soon as the MAPbI$_3$ precursor film comes in contact with DEE, the NMP solvent is extracted selectively because NMP is highly miscible in DEE. However, this occurs in localized patches in the very early stages (see Fig. S2†), most likely due to local variations in the composition of the film and/or in the nature of its contact with the DEE solvent. This triggers the crystallization of MAPbI$_3$ perovskite in areas devoid of NMP, which spreads rapidly to cover the entire area as NMP is fully extracted by DEE (Figs. S1† and S2†). Since MAPbI$_3$ perovskite is insoluble in non-polar DEE and the process is so rapid, the crystallized film is not damaged during this room-temperature process. Finally, the low boiling point of DEE (35 ˚C), compared to the precursor solvent NMP (204 ˚C), allows ambient drying to remove any remaining DEE solvent. Figure S3† shows that when drops (~2 mm in diameter) of MAPbI$_3$ precursor solution (in NMP), instead of the spin-coated thin film, are added to DEE solvent, the precipitation of MAPbI$_3$ perovskite appears to be extremely sluggish visibly. These observations suggest that the nanoscale of the thin film is critical to the success of the SSE process. The proposed SSE mechanisms discussed above is illustrated schematically in Figure 5E.

While the NMP/DEE precursor/extracting solvents combination used here is a typical example for the demonstration of the SSE method, a wide range of other solvents, or mixed solvents, could be used to suit the specific perovskite being deposited. The following general rules are suggested. (i) The precursor solvent (polar) must have high solubility for perovskite precursor, allowing deposition of films with wide range of uniform thicknesses, and a high boiling point, preventing evaporation-induced unbalanced perovskite growth and/or the formation of complexes. (ii) The extracting solvent (non-polar) must have no solubility for the perovskite precursors, must not react with the solid perovskites, and have a low boiling point (preferably <100 ˚C), allowing rapid drying in the ambient. (iii) The precursor solvent must be highly miscible in extracting solvent, and it must disperse rapidly in the large volume of the extracting solvent (bath), enabling rapid SSE deposition.

Solar cells based on SSE perovskite thin films

Figure 6A presents typical *J-V* curves (reverse scan) under simulated one-sun AM 1.5G (100 mW cm^{-2}) illumination of PSCs fabricated using SSE MAPbI$_3$ perovskite thin films of thickness ~20 nm, ~80 nm, and ~250 nm. The solar-cell performance parameters extracted from these data are presented in Table 1. When the perovskite film thickness is ~20 nm, the PSC exhibits a PCE of 4.1% with a short-circuit photocurrent density (J_{SC}) of 7.3 mA cm^{-2}, open-circuit voltage (V_{OC}) of 0.88 V, and fill factor (*FF*) of 0.638. The PCE increases to 10.1% and 13.4% when the perovskite film thickness is increased to ~80 and ~250 nm, respectively. The highest PCE recorded is 15.2% for a PSC with ~250 nm perovskite film thickness. The improved efficiency with increasing perovskite film thickness is mainly the result of the larger J_{SC} values associated with the increased optical absorption (see Fig. S8†). The J_{SC} values for these PSCs are consistent with their respective external quantum efficiency (EQE) spectra, which are shown in Fig. 6B. Since *J-V* hysteresis between forward (normal) and reverse scans is typically observed for SSE planar PSCs (see Fig. S9†), the stability of current output at maximum-power-point under continuous one-sun illumination was measured. Figure 7 shows that, for a typical PSC made using ~250 nm SSE MAPbI$_3$ perovskite thin film, the maximum power output stabilizes at

~13.2% over a couple of minutes, which compares favourably with the values obtained from the *J-V* measurements under reverse scan (Fig. 6A).

The mean, maximum, and minimum PCE values for 10-20 PSCs tested for each perovskite thickness are presented in Fig. S10†. The tight distribution of PCE values indicates that the SSE method for $MAPbI_3$ perovskite thin film deposition is reproducible. While the highest PCE of 15.2% is for PSCs based on ~250 nm SSE $MAPbI_3$ perovskite thin film, PCE of over 10% for PSCs made from a ~80-nm film is unprecedented, and it is attributed to the high quality of the perovskite thin films made possible by the SSE method. It is noteworthy that even when the film thickness is reduced down to ~20 nm, an average PCE of 4.1% is achieved, further attesting to the high quality of SSE $MAPbI_3$ perovskite thin films. These results indicate that ultra-thin SSE perovskite films hold promise for use in future PSCs demanding low lead content.

Impedance spectroscopy is used to investigate the effect of perovskite film thickness on the recombination resistance (R_{Recomb}) for perovskite solar cells based on $MAPbI_3$ thin films deposited using the SSE method. Figure S11A† shows typical impedance spectra (IS) in the complex plane for a PSCs based on ~250 nm SSE $MAPbI_3$ perovskite thin film under three different bias voltages. The IS for all three bias voltages are dominated by a large semicircle at low frequencies. This large semicircle is often attributed to the charge recombination process within the PSC. The model used for the analysis of the IS data has been discussed previously in detail.[25, 30, 31] Figure S11B† compares the recombination resistance R_{Recomb} as a function of voltage for PSCs with three different SSE $MAPbI_3$ film thicknesses. The R_{Recomb} for all three PSCs depends strongly on the bias voltage, following a similar voltage dependence as reported previously.[9] When compared at a fixed voltage, the R_{Recomb} values for the 20-nm film PSC are significantly smaller, by about a factor of 5-10, compared to those for PSCs with 80-250 nm SSE $MAPbI_3$ film thicknesses. A smaller R_{Recomb} corresponds to a faster recombination rate, which could account for the observed lower V_{OC} for the 20-nm film PSC compared to that for the 80- and 250-nm film PSCs.

In order to further demonstrate the robustness of the room-temperature SSE method, the as-deposited SSE $MAPbI_3$ thin films (~250 nm thickness) were annealed at 100 ˚C for 15 min in air. Initial results from the characterization of the annealed films, as seen in Fig. S12A† (XRD) and Fig. S12B† (SEM), do not show any obvious effects of annealing on the phase purity and the microstructure of the SSE $MAPbI_3$ thin films. This indicates complete crystallization of the $MAPbI_3$ perovskite in the SSE process. Consequently, annealing does not have a measureable effect on the PCEs of the PSCs made from those thin films (Fig. S13†). In contrast, other methods such as "solvent-engineering,"[14] FDC,[15] and solvent-washing[19] require post-deposition annealing to achieve high PCEs (>10%).

The SSE method is highly versatile, and we have used it for the room-temperature deposition of semi-transparent thin films of $MAPbI_{(3-x)}Br_x$ (x = 0, 1, 2, or 3) perovskites with different vivid colours (Fig. 8) and tuned bandgaps[32, 33] *via* composition control. Figure 8 also demonstrates the tailoring of semi-transparency of the $MAPbI_{(3-x)}Br_x$ perovskite thin films *via* thickness control. Furthermore, the room-temperature SSE method will allow the deposition of hybrid-perovskite thin films on a wide range substrate materials, for potential applications in flexible PSCs, building-integrated PSCs, and tandem photovoltaics. Finally, the key attributes of the SSE method — room-temperature process, rapid crystallization, large-area uniform deposition, film-thickness control, ultra-smoothness, and compositional versatility — make it potentially suitable for roll-to-roll scalable processing of hybrid-perovskite thin films for future multifunctional PSCs.

Conclusions

We have demonstrated the feasibility of the room-temperature SSE processing concept for the deposition of hybrid-perovskite thin films for PSCs. Insights into the SSE deposition mechanisms are provided, and we have shown that the SSE method uses the principle of solvent-extraction-induced crystallization during solvent bathing, enabling the rapid formation of ultra-smooth perovskite thin films with large-area uniformity. The planar PSCs fabricated using SSE MAPbI$_3$ perovskite films deliver PCE of up to 15.2%. Furthermore, the high quality of the perovskite films afforded by the SSE method allows the use of thinner, semi-transparent films (~80 nm) in PSCs delivering an unprecedented PCE of 10.1%. We have also demonstrated the versatility of the SSE method in depositing thin films of controlled thicknesses (20 to 700 nm) and various compositions (MAPbI$_{(3-x)}$Br$_x$; $x = 0$, 1, 2, or 3). The SSE method has generic appeal, and it is potentially suitable for roll-to-roll scalable processing of hybrid-perovskite thin films for future multifunctional PSCs.

Acknowledgements

References

1. H. J. Snaith, *J. Phys. Chem. Lett.*, 2013, **4**, 3623-3630.
2. M. Grätzel, *Nature Mater.*, 2014, **13**, 838-842.
3. M. A. Green, A. Ho-Baillie and H. J. Snaith, *Nature Photon.*, 2014, **8**, 506-513.
4. M. He, D. Zheng, M. Wang, C. Lin and Z. Lin, *J. Mater. Chem. A*, 2014, **2**, 5994-6003.
5. H. S. Jung and N.-G. Park, *Small*, 2015, **11**, 10-25.
6. NREL, *www.nrel.gov/ncpv/images/efficiency_chart.jpg*, 2014.
7. D. B. Mitzi, in *Progress in Inorganic Chemistry*, Ed. K. D. Karlin, John Wiley & Sons, New York, NY, 1999, pp. 1-122.
8. A. Kojima, K. Teshima, Y. Shirai and T. Miyasaka, *J. Am. Chem. Soc.*, 2009, **131**, 6050-6051.
9. H.-S. Kim, C.-R. Lee, J.-H. Im, K.-B. Lee, T. Moehl, A. Marchioro, S.-J. Moon, R. Humphrey-Baker, J.-H. Yum, J. E. Moser, M. Grätzel and N.-G. Park, *Sci. Rep.*, 2012, **2**, 591.
10. J.-H. Im, H.-S. Kim and N.-G. Park, *APL Mater.*, 2014, **2**, 081510.
11. Y. Zhao and K. Zhu, *J. Phys. Chem. Lett.*, 2014, **5**, 4175-4186.
12. J. Burschka, N. Pellet, S.-J. Moon, R. Humphrey-Baker, P. Gao, M. K. Nazeeruddin and M. Gratzel, *Nature*, 2013, 499, 316-319.
13. Z. Xiao, C. Bi, Y. Shao, Q. Dong, Y. Yuan, C. Wang, Y. Gao and J. Huang, *Ener. Environ. Sci.*, 2014, **7**, 2619-2623.
14. N. J. Jeon, J. H. Noh, Y. C. Kim, W. S. Yang, S. Ryu and S. I. Seok, *Nature Mater.*, 2014, **9**, 897-903.

15. M. Xiao, F. Huang, W. Huang, Y. Dkhissi, Y. Zhu, J. Etheridge, A. Gray-Weale, U. Bach, Y.-B. Cheng and L. Spiccia, *Ange. Chem. Intl. Ed.*, 2014, **53**, 9898-9903.
16. F. Huang, Y. Dkhissi, W. Huang, M. Xiao, I. Benesperi, S. Rubanov, Y. Zhu, X. Lin, L. Jiang, Y. Zhou, A. Gray-Weale, J. Etheridge, C. McNeill, R. A. Garuso, U. Bach, L. Spiccia and Y.-B. Cheng, *Nano Ener.*, 2014, **10**, 10-18.
17. Y. Kutes, L. Ye, Y. Zhou, S. Pang, B. D. Huey and N. P. Padture, *J. Phys. Chem. Lett.*, 2014, **5**, 3335-3339.
18. Y. Zhou, M. Yang, A. L. Vasiliev, H. F. Garces, Y. Zhao, D. Wang, S. Pang, K. Zhu and N. P. Padture, *J. Mater. Chem. A*, 2015, in press, doi: 10.1039/C4TA07036D.
19. J. W. Jung, S. T. Williams and A. K.-Y. Jen, *RSC Adv.*, 2014, in press, doi: 10.1039/C4RA13212B.
20. H. Hu, D. Wang, Y. Zhou, J. Zhang, S. Lv, S. Pang, X. Chen, Z. Liu, N. P. Padture and G. Cui, *RSC Adv.*, 2014, **4**, 28964-28967.
21. M. Liu, M. B. Johnston and H. J. Snaith, *Nature*, 2013, 501, 395-398.
22. O. Malinkiewicz, A. Yella, Y. H. Lee, G. M. Espallargas, M. Gratzel, M. K. Nazeeruddin and H. J. Bolnik, *Nature Photon.*, 2013, **8**, 128-132.
23. Q. Chen, H. Zhou, Z. Hong, S. Luo, H.-S. Duan, H.-H. Wang, Y. Liu, G. Li and Y. Yang, *J. Am. Chem. Soc.*, 2014, **136**, 622-625.
24. F. Hao, C. C. Stoumpos, Z. Liu, R. P. H. Chang and M. G. Kanatzidis, *J. Am. Chem. Soc.*, 2014, in press, doi: 10.1021/ja509245x.
25. M. M. Lee, J. Teuscher, T. Miyasaka, T. N. Murakami and H. J. Snaith, *Science*, 2012, **338**, 643-647.
26. H. J. Snaith, A. Abate, J. M. Ball, G. F. Eperon, T. Leijtens, N. K. Noel, S. D. Stranks, J. T.-W. Wang, K. Wojciechowski and W. Zhang, *J. Phys. Chem. Lett.*, 2014, **5**, 1511-1515.
27. C. C. Stoumpos, C. D. Malliakas and M. G. Kanatzidis, *Inorg. Chem.*, 2013, **52**, 9019-9038.
28. V. S. Kislik, *Solvent Extraction: Classical and Novel Approaches*, Elsevier, Oxford, UK, 2011.
29. NIST, http://webbook.nist.gov/cgi/cbook.cgi?ID=C872504&Mask=80#IR-Spec.
30. J. A. Christians, R. C. M. Fung and P. V. Kamat, *J. Am. Chem. Soc.*, 2014, **136**, 758-764.
31. E. J. Juarez-Perez, M. Wussler, F. Fabregat-Santiago, K. Lakus-Wollny, E. Mankel, T. Mayer, W. Jaegermann and I. Mora-Sero, *J. Phys. Chem. Lett.*, 2014, **5**, 680-685.
32. J. H. Noh, S. H. Im, J. H. Heo, T. N. Mandal and S. I. Seok, *Nano Lett.*, 2013, **13**, 1764-1769.
33. Y. Zhao and K. Zhu, *J. Am. Chem. Soc.*, 2014, **136**, 12241-12244.

**Table 1.** Solar cell performance parameters extracted from the *J-V* characteristics in Fig. 4A.

| SSE Perovskite Film Thickness	J_{SC} (mA cm^{-2})	*FF*	V_{OC} (V)	PCE (%)
20 nm	7.3	0.638	0.88	4.1
80 nm	14.1	0.663	1.08	10.1
250 nm	19.0	0.659	1.07	13.4
250 nm*	20.7	0.680	1.08	15.2

* Solar cell with highest PCE.

Figure Captions

1. Schematic illustration showing the SSE process for the all-room-temperature deposition of hybrid-perovskite thin films.

2. (A) Indexed XRD pattern, and (B) low- and (C) high-magnification SEM micrographs of the top surface of a MAPbI$_3$ perovskite film (~250 nm thickness) deposited on a glass substrate using the SSE method.

3. Cross-sectional images of MAPbI$_3$ perovskite films deposited on TiO$_2$-blocking-layer coated FTO-glass substrates: (A) SEM (~250 nm film thickness) and (B) bright-field TEM (~80 nm film thickness). The light contrast at the interface between the FTO and the perovskite in (B) is the TiO$_2$ blocking layer. (C) Plan-view high-resolution TEM images of a MAPbI$_3$ perovskite film deposited on a TEM grid using the SSE method showing lattice fringes and defects, and (D) higher magnification image of area marked by red rectangle in (C) showing ~0.44 nm (020) and ~0.32 nm (004) spaced planes.

4. AFM images of a MAPbI$_3$ perovskite film (~250 nm thickness) deposited on a TiO$_2$-blocking-layer coated FTO-glass substrate: (A) large area (40×40 μm^2) and (B) smaller area (2×2 μm^2). (C) Photograph of a MAPbI$_3$ perovskite film (~250 nm thickness) deposited on a TiO$_2$-blocking-layer coated FTO-glass substrate (dashed 5×6 cm^2 rectangle) held in bright sunshine. (D) Photograph of the same film showing high reflectivity.

5. XRD patterns from: (A) MAPbI$_3$ precursor as-spin-coated film (in NMP) on a glass substrate, and (B) after 2 s and (C) after 2 min of NMP extraction by DEE solvent at room temperature. Note the sharpening of the XRD peaks in (C). (D) FTIR spectra corresponding to (B) 2 s (red) and (C) 2 min (black). The C=O stretching band at ~1700 cm^{-1} observed in the 2-s film is marked in (D). (E) Schematic illustration of the proposed SSE deposition mechanisms.

6. (A) *J-V* characteristics of PSCs based on MAPbI$_3$ perovskite thin films with different thicknesses deposited by SSE at room temperature, under simulated one-sun AM 1.5G (100 mW cm^{-2}) illumination. The dashed red *J-V* curve is for a PSC with the highest PCE of 15.2%. (B) External quantum efficiency (EQE) as a function of wavelength for the PSCs in (A).

7. Stability of *J* and PCE as a function of time for a PSC based on SEE MAPbI$_3$ perovskite thin film (~250 nm thickness) under simulated one-sun AM 1.5G (100 mW cm^{-2}) illumination.

8. Photograph of MAPbI$_{(3-x)}$Br$_x$ perovskite films deposited on TiO$_2$-blocking-layer coated FTO-glass substrates using the SSE process at room temperature for different *x* (0, 1, 2, 3) and film thicknesses (~20 nm, ~80 nm, ~250 nm, ~400 nm), demonstrating that the semi-transparency and color can be tuned through these variables.
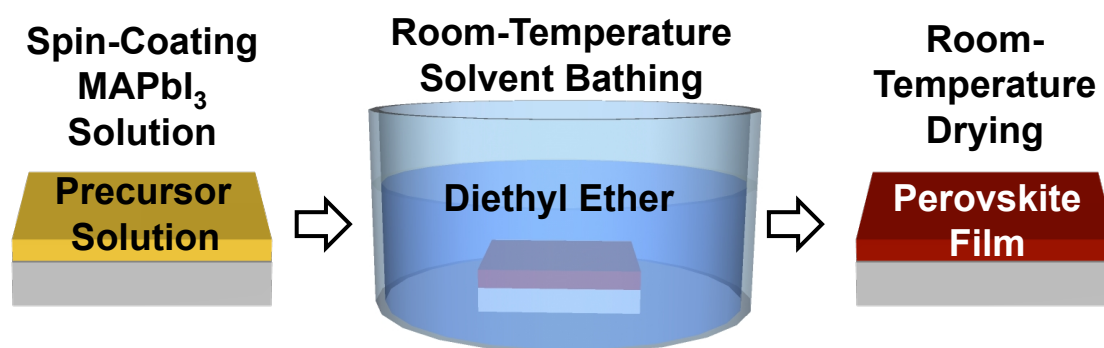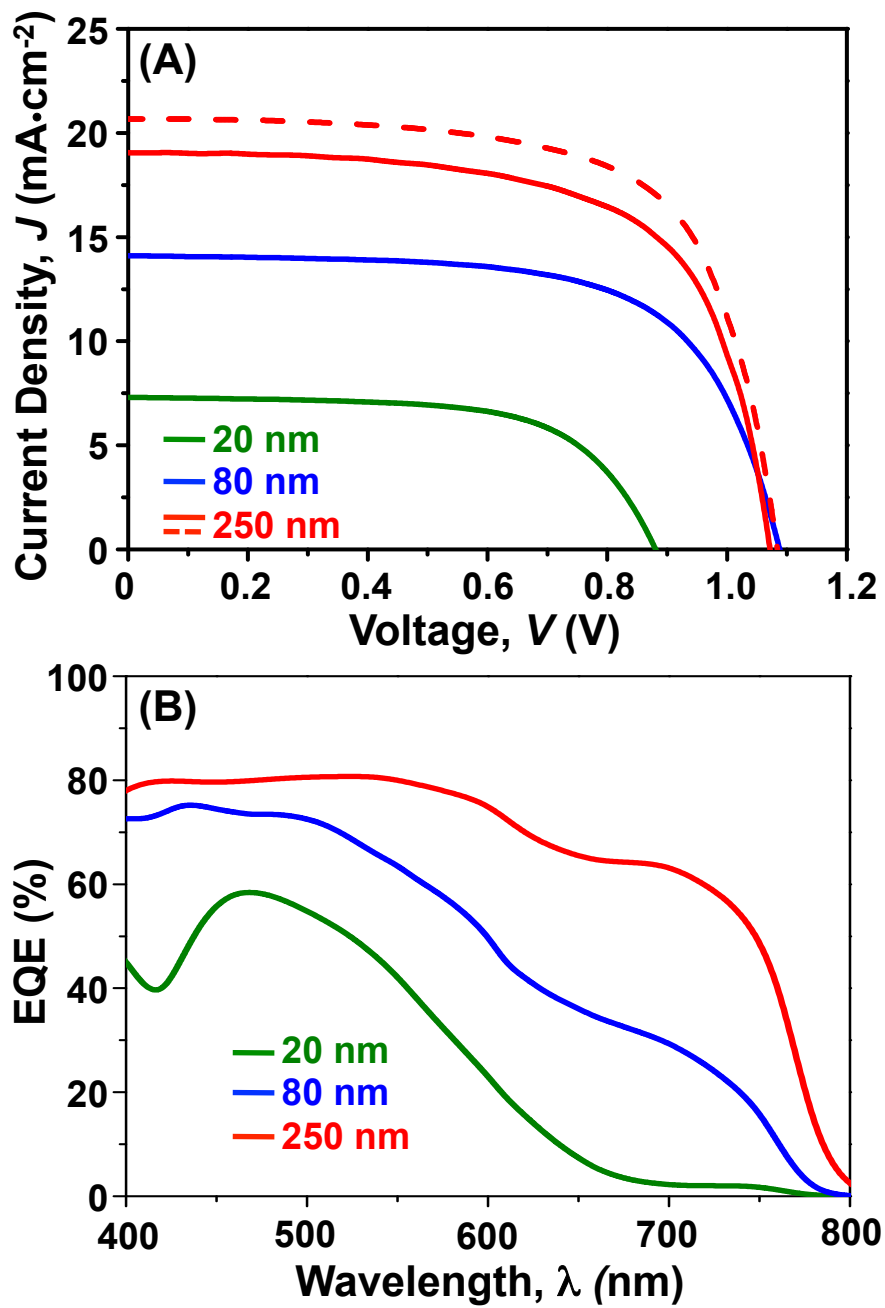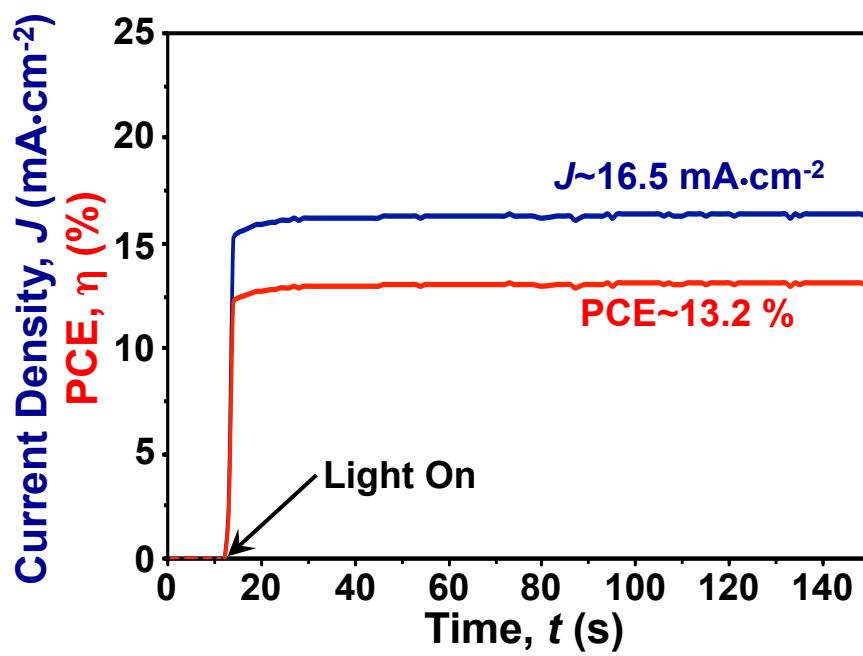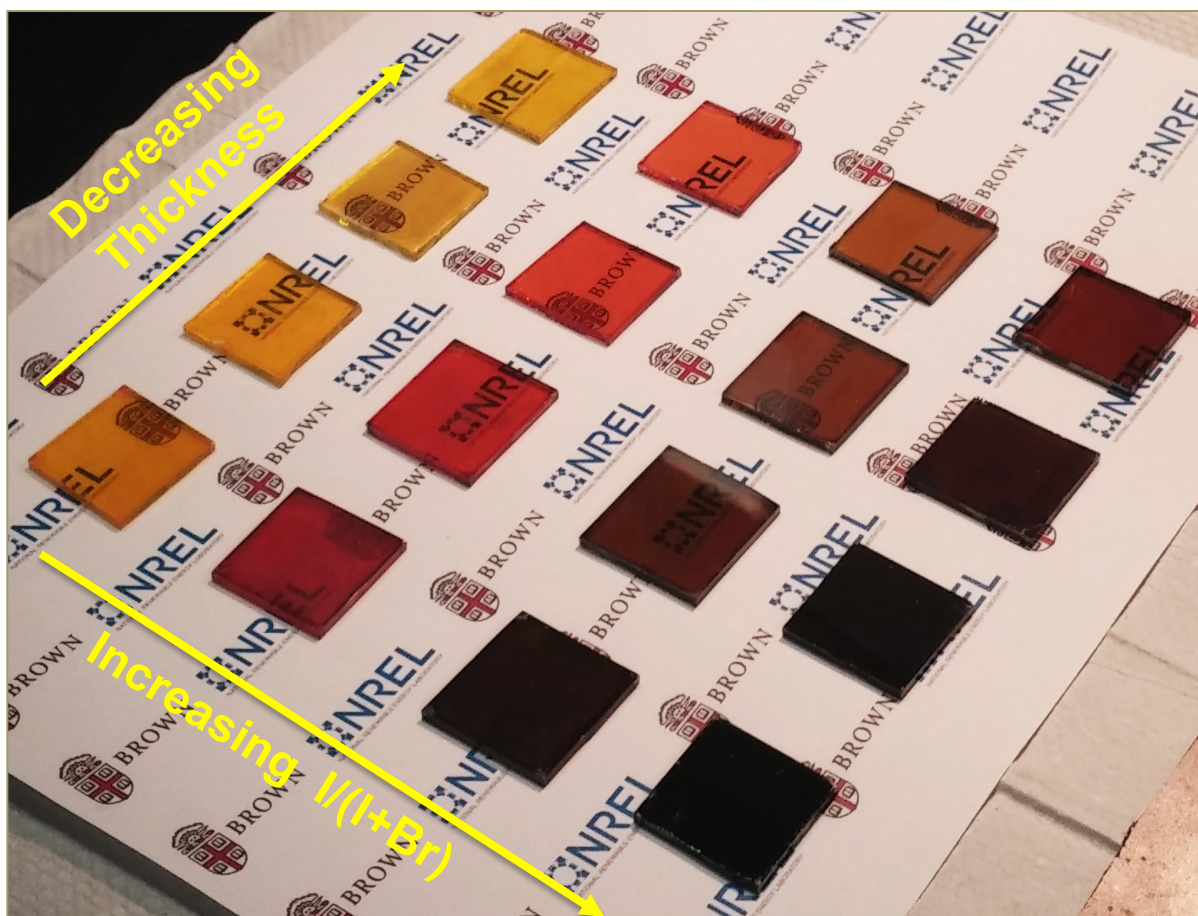
Fig. 1, Zhou *et al.*
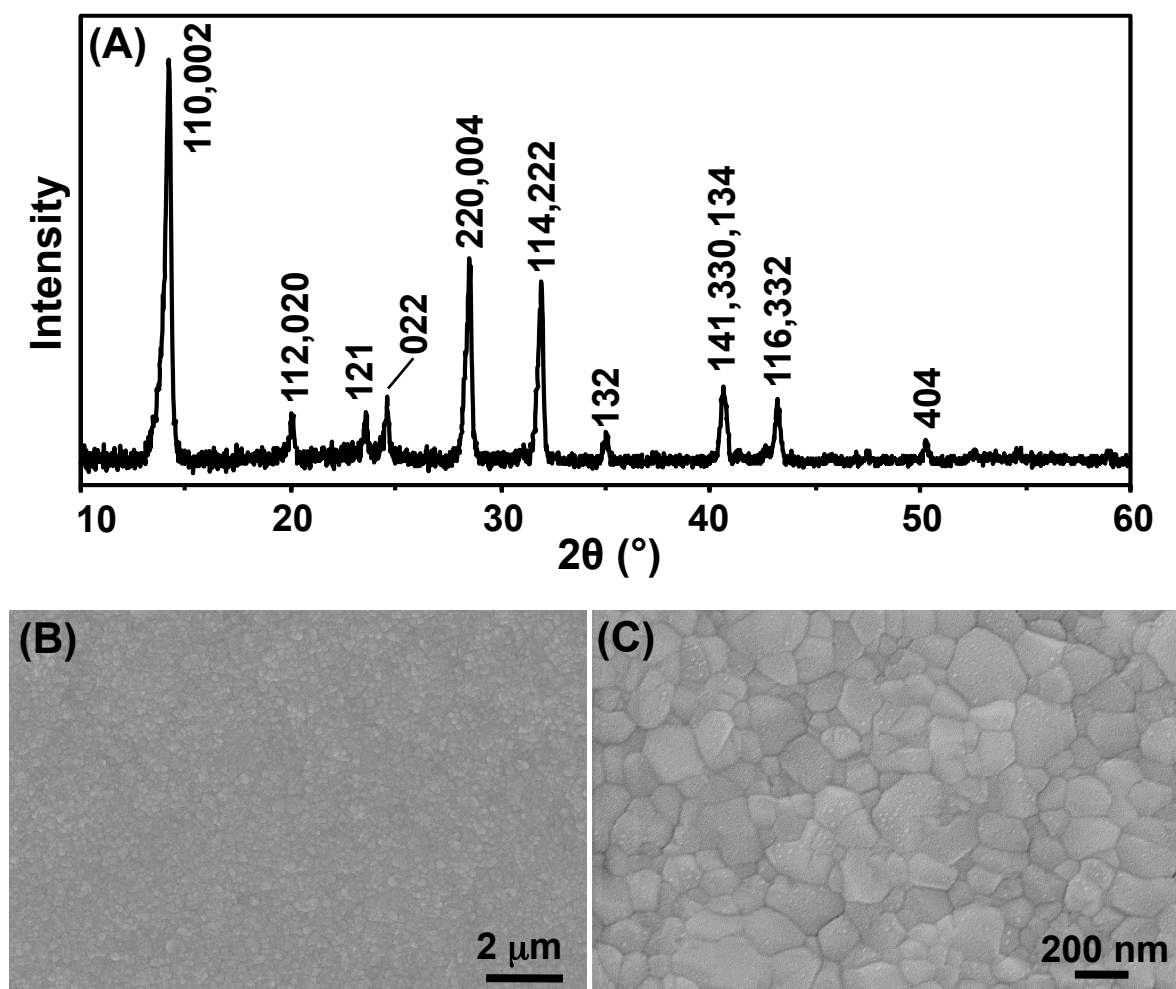
Fig. 2, Zhou *et al.*
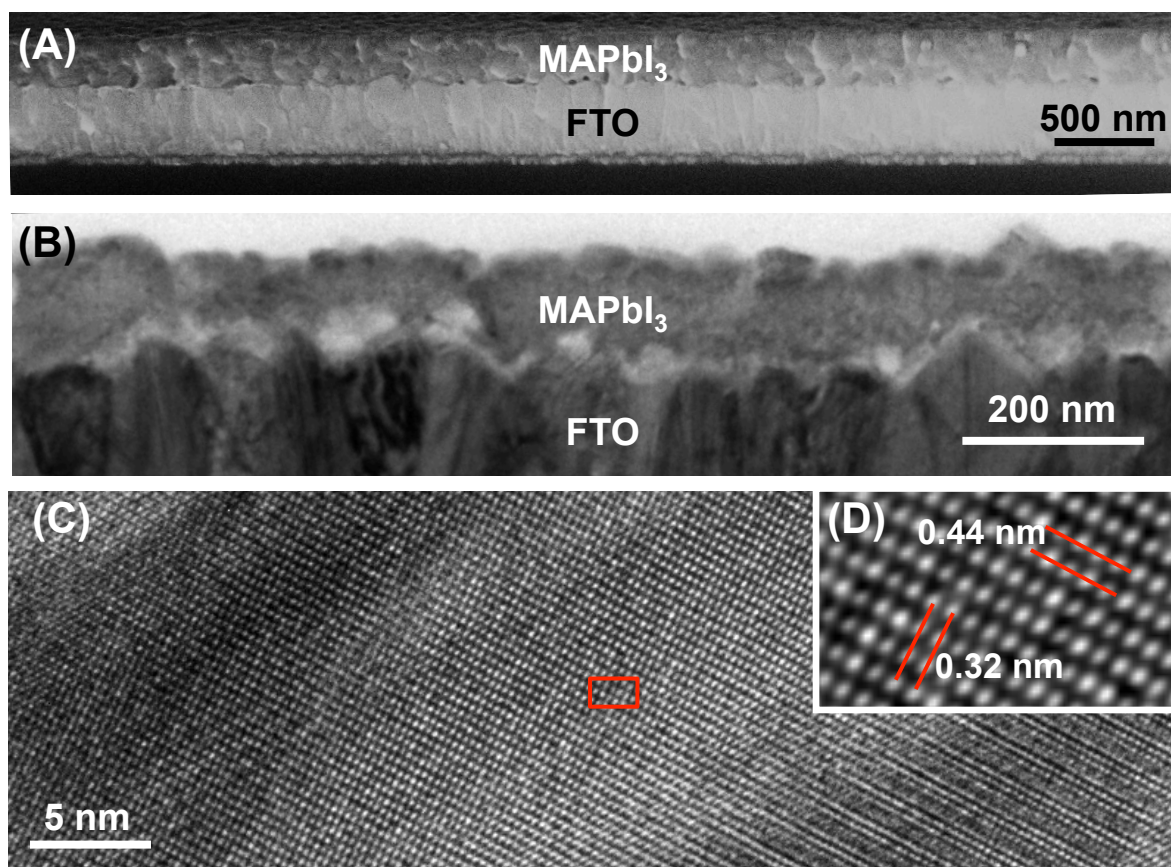
Fig. 3, Zhou *et al.*
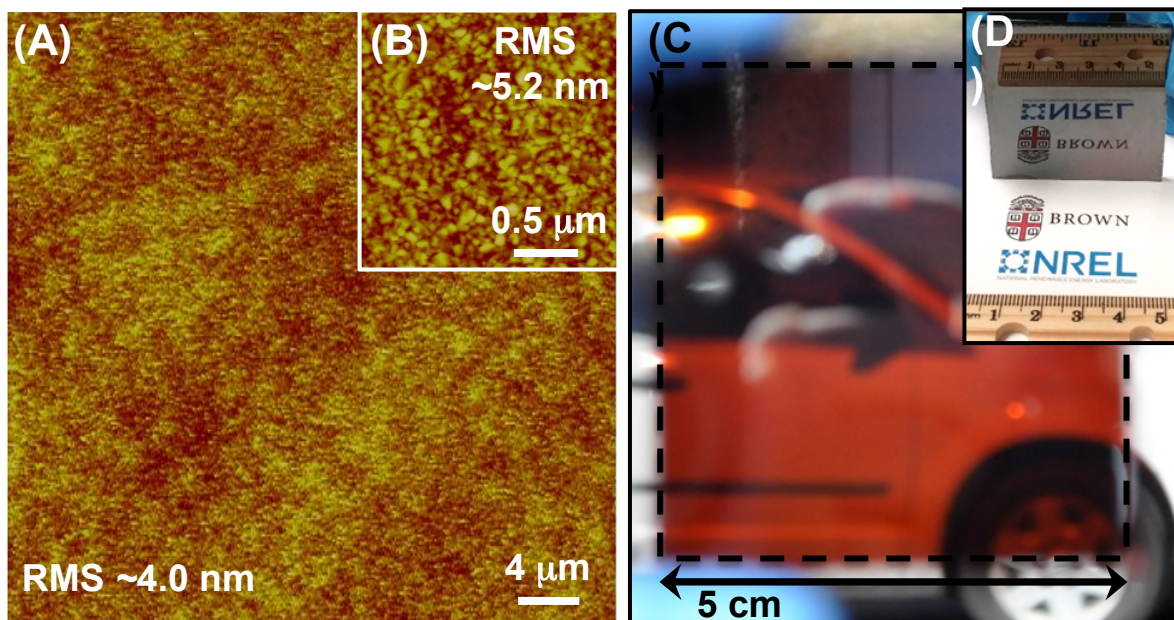
Fig. 4, Zhou *et al.*
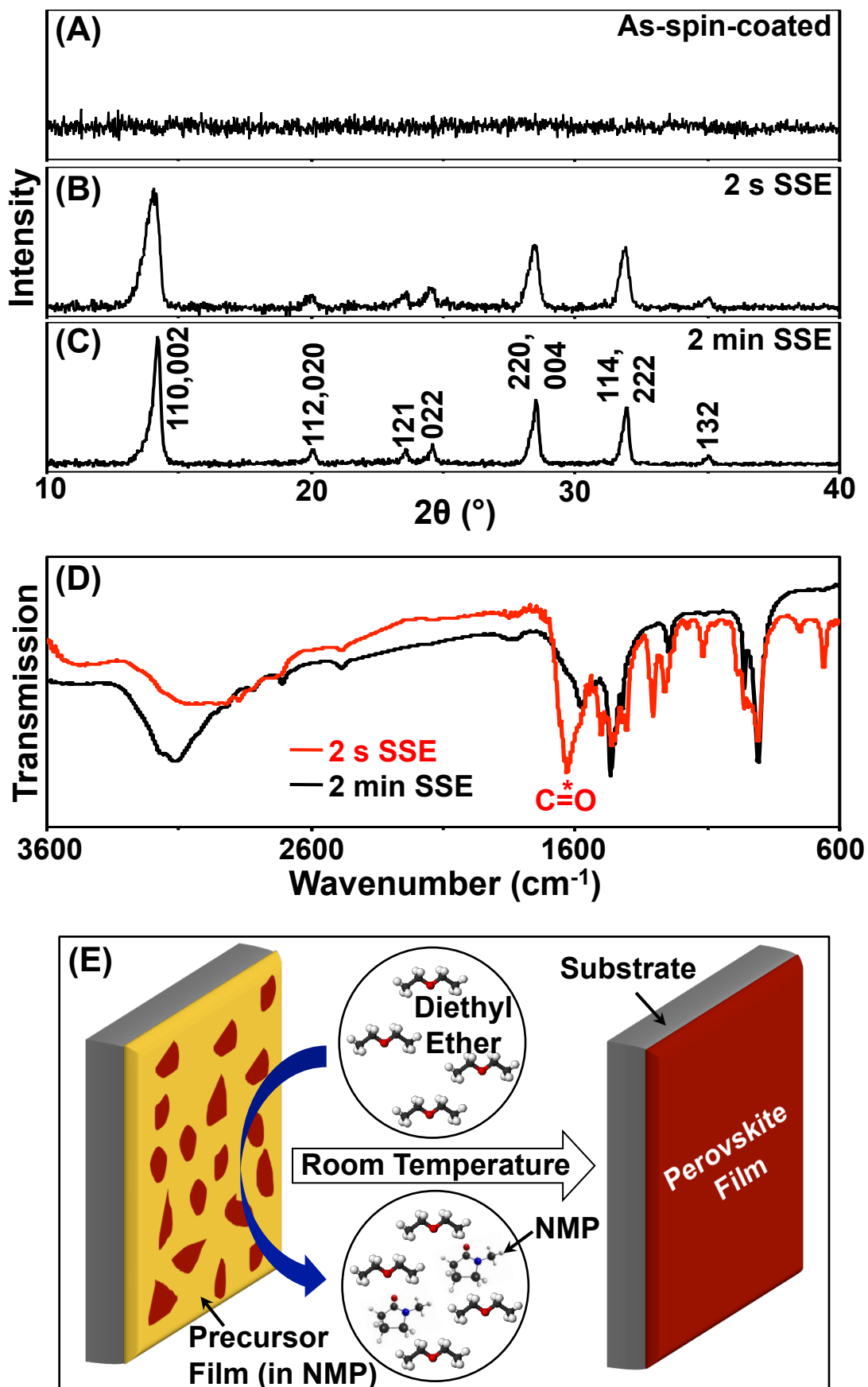
Fig. 5, Zhou *et al.*

Fig. 6, Zhou *et al.*

Fig. 7, Zhou *et al.*

Fig. 8, Zhou *et al.*